#### **ENGINEERING**

# Biodegradable silicon nanoneedles for ocular drug delivery

Woohyun Park<sup>1</sup>†, Van Phuc Nguyen<sup>2</sup>†, Yale Jeon<sup>3</sup>†, Bongjoong Kim<sup>4,5</sup>, Yanxiu Li<sup>2</sup>, Jonghun Yi<sup>3</sup>, Hyungjun Kim<sup>4,6</sup>, Jung Woo Leem<sup>4</sup>, Young L. Kim<sup>4</sup>, Dong Rip Kim<sup>3\*</sup>, Yannis M. Paulus<sup>2,7\*</sup>, Chi Hwan Lee<sup>1,4,8,9\*</sup>

Ocular drug delivery remains a grand challenge due to the complex structure of the eye. Here, we introduce a unique platform of ocular drug delivery through the integration of silicon nanoneedles with a tear-soluble contact lens. The silicon nanoneedles can penetrate into the cornea in a minimally invasive manner and then undergo gradual degradation over the course of months, enabling painless and long-term sustained delivery of ocular drugs. The tear-soluble contact lens can fit a variety of corneal sizes and then quickly dissolve in tear fluid within a minute, enabling an initial burst release of anti-inflammatory drugs. We demonstrated the utility of this platform in effectively treating a chronic ocular disease, such as corneal neovascularization, in a rabbit model without showing a notable side effect over current standard therapies. This platform could also be useful in treating other chronic ocular diseases.

Copyright © 2022
The Authors, some rights reserved; exclusive licensee
American Association for the Advancement of Science. No claim to original U.S. Government Works. Distributed under a Creative
Commons Attribution
NonCommercial
License 4.0 (CC BY-NC).

#### INTRODUCTION

Most common routes of ocular drug delivery rely on topical eye administration using either eye drops or ointments, but their bioavailability is limited typically to below 5% due to the presence of ocular barriers (1-4). Thereby, current therapeutic regimes often require a large dose or frequent topical applications, which burdens patients and also increases the risk of side effects such as keratitis, blurred vision, and eye discomfort (5). Continued innovation of microneedles has synergistically advanced the field of ocular drug delivery over the past decades, enabling a targeted injection of ocular drugs through the ocular barriers to enhance therapeutic efficacy (6). However, the clinical implementation of the microneedles in human eyes remains challenged due to their relatively large size in a submillimeter range and the exceptional sensitivity of the cornea (i.e., corneal pain). The submillimeter size of the microneedles may also result in corneal damage (7). Recent efforts have enabled the phenomenal success of producing further miniaturized (i.e., down to 250 µm in base diameter) and biodegradable microneedles for painless drug delivery with reduced side effects (8-11). Despite great advances, their long-term therapeutic efficacy is limited due to the rapidly dissolving nature (i.e., burst release) of biodegradable composites, such as poly(lactic-co-glycolic) acid (PLGA) and methacrylate hyaluronic acid (MeHA), in a range of 24 to 120 μm day<sup>-1</sup>. This limitation is particularly problematic in treating chronic ocular

diseases, such as corneal neovascularization (CNV), which can benefit from long-term sustained drug delivery.

Vertically ordered arrays of silicon nanoneedles (Si NNs), because of their nanoscale size, low toxicity, and slow biodegradability (i.e., <20 nm day<sup>-1</sup> in physiological conditions), are of particular interest for minimally invasive and long-term sustained drug delivery (12–14). For therapeutic delivery, the surface of Si NNs can be functionalized to accommodate various drug molecules such as steroids, hormones, proteins, and anticancer agents, and then injected percutaneously or intraperitoneally in humans without notable side effects (15). However, current Si NNs are necessarily bound to a flat, rigid Si wafer due to the complexity of nanofabrication, which would inevitably result in mechanical mismatch (i.e., discomfort and pain) particularly when interfaced with the curvilinear, soft surface of the cornea. Because of these challenges, none of these Si NNs have been applied to the human eye. Thus, there is an unmet need to unlock the fundamental limit of Si NNs in a substrate-free environment, thereby extending their applicability even to the human eye.

To this end, we developed a vertically ordered array of biodegradable Si NNs on a tear-soluble contact lens, enabling many advances in ocular drug delivery over typical biodegradable composites (e.g., PLGA and MeHA). Specifically, Si NNs offer the following unique features: (i) at least five orders of magnitude larger mechanical stiffness (E = 112.4 GPa) with sharpened tips for reliable penetration through the corneal barriers while causing minimal corneal damage, (ii) at least 80-fold smaller size in base diameter for painless injection, (iii) at least five orders of magnitude prolonged degradation in tear fluid for long-term sustained drug delivery, (iv) nanoscale surface porosity for precise dosage adjustment, and (v) strong covalent binding affinity of drug molecules along the surface for leakage-free drug loading. In parallel, the tear-soluble contact lens offers the following unique features: (i) sufficiently large mechanical stiffness (E = 4 GPa) for easy lens handling and fitting, (ii) medical-grade biocompatibility for minimal side effects, (iii) optimal curvature (8.3 to 9.0 mm in base curve radii) to fit a variety of corneal sizes for seamless fitting, (iv) rapid dissolution and complete wash away with tear fluid for user comfort without visual disturbance, and (v) drug reservoir to enable an initial burst release of

<sup>&</sup>lt;sup>1</sup>School of Mechanical Engineering, Purdue University, West Lafayette, IN 47907, USA. <sup>2</sup>Department of Ophthalmology and Visual Sciences, University of Michigan, Ann Arbor, MI 48105, USA. <sup>3</sup>School of Mechanical Engineering, Hanyang University, Seoul 04763, Republic of Korea. <sup>4</sup>Weldon School of Biomedical Engineering, Purdue University, West Lafayette, IN 47907, USA. <sup>5</sup>Department of Mechanical and System Design Engineering, Hongik University, Seoul 04066, Republic of Korea. <sup>6</sup>Department of Applied Chemistry, Kumoh National Institute of Technology, Gumi, Gyeongbuk 39177, Republic of Korea. <sup>7</sup>Department of Biomedical Engineering, University of Michigan, Ann Arbor, MI 48105, USA. <sup>8</sup>Department of Materials Engineering, Purdue University, West Lafayette, IN 47907, USA. <sup>9</sup>Birck Nanotechnology Center, Purdue University, West Lafayette, IN 47907, USA.

<sup>\*</sup>Corresponding author. Email: dongrip@hanyang.ac.kr (D.R.K.); ypaulus@med. umich.edu (Y.M.P.); lee2270@purdue.edu (C.H.L.)

<sup>†</sup>These authors contributed equally to this work.

anti-inflammatory or other ocular drugs of interest for enhanced therapeutic efficacy. We conducted comprehensive studies in vitro, ex vivo, and in vivo not only to reveal the underlying properties of the resulting platform but also to validate its therapeutic efficacy and biosafety in a rabbit CNV model as compared to subconjunctival injection and surgical therapies.

#### **RESULTS**

#### Platform design and production

The fabrication of Si NNs began with a Si wafer using a standard photolithographic patterning process, followed by a series of dry and wet etching processes to form undercuts and pores at the bottom root and along the surface, respectively (fig. S1). Details of the fabrication process are described in Materials and Methods. The geometric configuration of Si NNs was controlled in terms of the base diameter (i.e., >900 nm), aspect ratio (i.e., 2 to 67), and surface porosity (i.e., 0 to 60%) (fig. S2). Figure 1 provides schematic illustrations

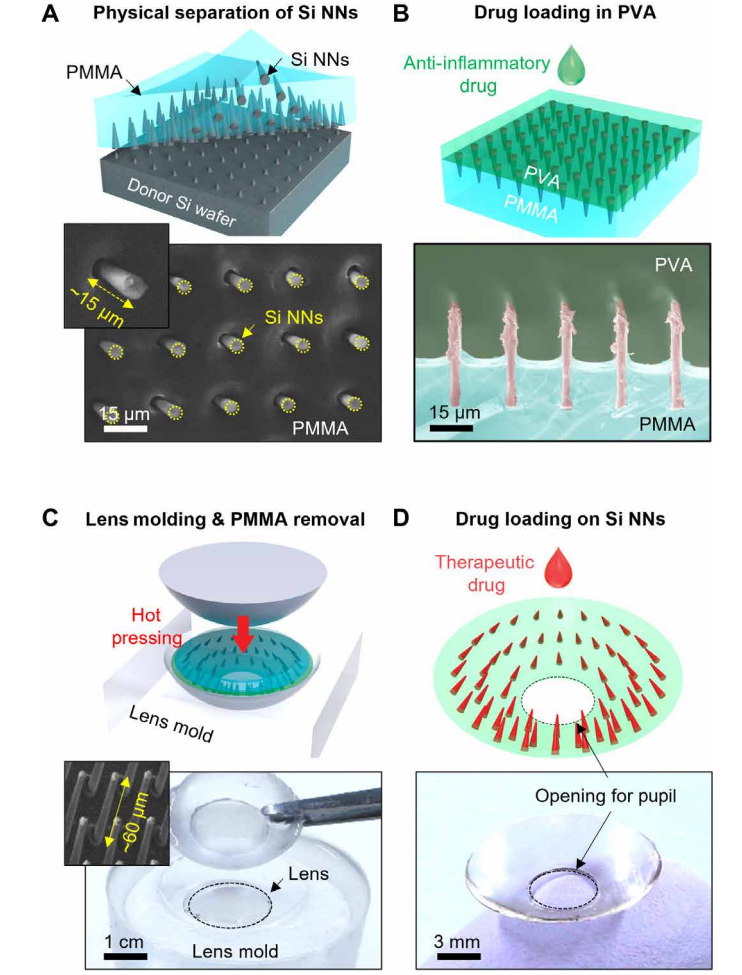


**Fig. 1. Platform design and production.** Schematic illustrations (top) and optical images (bottom) for the basic procedures regarding the physical transfer of the asprepared Si NNs from the Si wafer to a tear-soluble contact lens, including (**A**) the transfer of Si NNs to a PMMA film, (**B**) the deposition of a water-soluble film with anti-inflammatory drug, (**C**) the hot pressing of the resulting structure into a lens-shaped mold, and (**D**) the loading of therapeutic drugs to the surface of Si NNs.

(top) and optical images (bottom) for the subsequent transfer process of the as-prepared Si NNs from the donor Si wafer to a tear-soluble contact lens. First, a thin layer (200 µm thick) of polymethyl methacrylate (PMMA) was coated over Si NNs, followed by a mechanical peeling at a constant rate of 50 mm min<sup>-1</sup> using an automated peeling apparatus (Mark-10; Willrich Precision Instrument) (Fig. 1A). During this peeling process, mechanical stresses were intensively concentrated at the bottom undercuts of Si NNs to generate cracks, leading to their physical separation from the donor Si wafer (16). The scanning electron microscopy (SEM) images (bottom) highlight the uniformly cracked Si NNs at the bottom undercuts with the exposed length of ~15 µm. Second, a water-soluble polyvinyl alcohol (PVA) solution diluted in distilled water [2 weight % (wt %)] was coated across the exposed surface, followed by a thermal annealing at 60°C for an hour to complete the polymerization (Fig. 1B). The cross-sectional colored SEM image (bottom) highlights the polymerized PVA film covering the entire Si NNs. For enhanced therapeutic efficacy, the PVA film could be mixed with an anti-inflammatory drug at this stage to enable a biphasic drug release (i.e., initial quick release of an anti-inflammatory drug from the tear-soluble contact lens followed by a long-term sustained release of a therapeutic ocular drug from Si NNs) (8). Third, the entire structure (i.e., PMMA/Si NNs/PVA) was trimmed into a circular shape (10 to 15 mm in diameter) and then pressed into a contact lens-shaped mold at 90°C for 5 min (Fig. 1C). The contact lens shape was obtained from several commercial artificial eyes that exhibit base curve radii ranging from 8.3 to 9.0 mm (fig. S3). The PMMA layer was then selectively removed with acetone. The inset SEM (bottom) highlights the exposed Si NNs from the PVA surface. The length of the exposed Si NNs (~60 µm) was matched within the maximum injectable depth (i.e., 43 to 63 µm) corresponding to the human corneal epithelial layer (i.e., ~50 μm thick) without causing irreversible corneal stromal scarring (17). The overall yield of this transfer process was ≥98% across the entire lens surface wherein some minor defects and Si debris appeared in arbitrary locations (fig. S4). Last, the surface of Si NNs was chemically functionalized with silane to form a strong covalent cross-linker to an antibody therapeutic ocular drug of interest (Fig. 1D). The photograph (bottom) shows the tear-soluble contact lens on which a hole (2 to 8 mm in diameter) was punched at the central visual axis (i.e., pupil area) to minimize corneal stromal haze. The thickness of the tear-soluble contact lens was controlled in a range of 37 to 43 µm, which is thinner than standard commercial contact lenses (50 to 180 µm thick). The mechanical integrity of the tear-soluble contact lens was maintained without any evidence of degradation over 6 months in a desiccator under ambient conditions (fig. S5). The optical transmission and haze of the tear-soluble contact lens were comparable or slightly higher compared to those of a commercial soft contact lens (Frequency 55 Aspheric; CooperVision Inc.) in visible spectrum (i.e., 400 to 700 nm) (fig. S6).

#### Working principle and control strategy

Figure 2A schematically illustrates the working principle of Si NNs in ocular drug delivery. Si NNs can be introduced into the corneal epithelial layer by gently pressing the tear-soluble contact lens onto the eye (Fig. 2A, left). The tear-soluble contact lens is then completely dissolved in tear fluid within less than a minute, through which an initial burst release of anti-inflammatory or other ocular drugs is carried out (Fig. 2A, middle). In parallel, the embedded Si

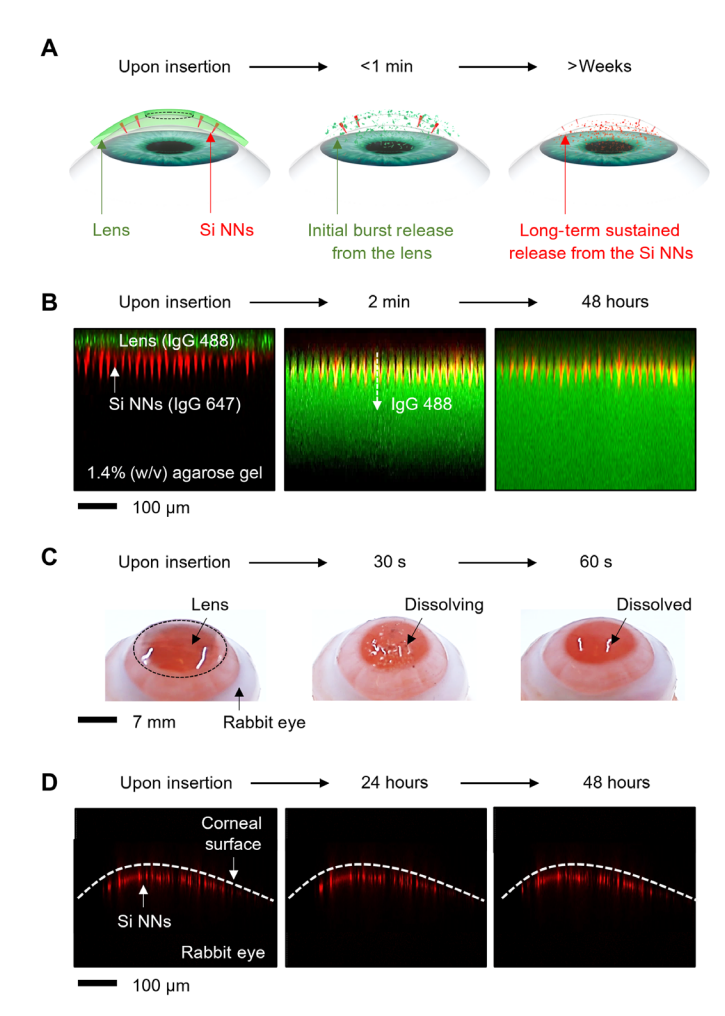


**Fig. 2. Working principle and control strategy.** (A) Time-lapse schematic illustrations of the biphasic drug delivery process. (B) Time-lapse confocal fluorescence microscopy images for the biphasic release of IgG 488 (green) and 647 (red) from the tear-soluble contact lens and Si NNs, respectively. (C) Time-lapse photographs of the enucleated rabbit eye with the tear-soluble contact lens while being dissolved. (D) Time-lapse cross-sectional confocal fluorescence microscopy images of the enucleated rabbit eye with Si NNs embedded into the cornea.

NNs are gradually dissolved in the cornea for a long period of time (i.e., over a month) via hydrolysis reaction of Si NNs into silicic acid and hydrogen in tear fluid (18–20), through which a long-term sustained release of therapeutic drugs is carried out (Fig. 2A, right). Figure 2B presents a series of confocal fluorescence microscopy images to visualize the biphasic drug release process using immunoglobulins (IgGs) labeled with Alexa Fluor 488 (green) and 647 (red) from the tear-soluble contact lens and Si NNs, respectively. Here, a 1.4% (w/v) agarose gel containing 1 ml of simulated tear fluid was used to surrogate the human cornea in mechanical stiffness  $(E \approx 20 \text{ kPa})$  and tear contents (>80%) (8). The detailed chemical composition of the simulated tear fluid is described in Materials and Methods. The results show that the initial burst release of IgG 488 (green) occurred within a minute after the dissolution of the tear-soluble contact lens, while the release of IgG 647 (red) barely appeared over 48 hours.

Figure 2C presents the corresponding ex vivo results with an enucleated rabbit eye that provides anatomical similarity to the

human eye in corneal thickness (540 to 560 µm) and curvature (8.3 to 9.0 mm in base curve radius) (21). The tear-soluble contact lens was gently pressed onto the rabbit eye and then completely dissolved within a minute in the simulated tear fluid. The overall size of the tear-soluble contact lens was adjustable to fit a variety of corneal sizes including the chicken eye (10 mm in diameter; 5.2 mm in base curve radius), pig eye (14 mm in diameter; 9 mm in base curve radius), and cow eye (30 mm in diameter; 15 mm in base curve radius) (fig. S7). Si NNs were invisible across the corneal surface owing to the nanoscale size effect, thereby inducing no noticeable corneal punctures. The confocal fluorescence microscopy in Fig. 2D confirms that the entire length (i.e., 60 µm long) of Si NNs remained plugged in the cornea without being washed away. The results also confirm that most of IgG 647 (red) remained at the surface of Si NNs over 48 hours, implying that the precorneal drug residence time was substantially prolonged comparing to topical eye drops (i.e., 1 to 30 min) and ointments (i.e., 1 to 8 hours) (22-24). All experiments in the enucleated eyes were completed within a day to minimize the effect of their decomposition over time.

#### **Drug loading mechanism and controls**

Covalent loading of therapeutic ocular drugs to the surface of Si NNs is integral to providing a strong binding affinity for leakage-free drug release. To this end, the surface of Si NNs was treated with 3-triethoxysilylpropyl succinic anhydride (TESPSA; Gelest) to form an amide type of covalent bonding to antibody ocular drugs such as the anti-vascular endothelial growth factor (VEGF) bevacizumab (Bev) (25, 26). Details of the drug loading process are described in Materials and Methods. Here, IgG was used to surrogate Bev according to their structural similarity, thereby also enabling the optical observation and quantification of the drug release process (8). Figure 3A provides a representative confocal fluorescence microscopy image, showing that IgG 647 (red) was uniformly loaded across the surface of Si NNs via covalent bonding. IgG 488 (green) was physically encapsulated (i.e., physical loading) in the tear-soluble contact lens with negligible residues of IgG 647 (red). Figure 3B provides a colored SEM image of the single Si NN, along with the schematic illustration of the drug loading mechanisms. The drug loading capacity was controllable through the modulation of either the surface porosity or size of Si NNs. For instance, the dosage of IgG 647 increased from  $10.17 \pm 0.70$  to  $17.44 \pm 0.74$  µg as the surface porosity of Si NNs increased from 0 to 60% at the fixed length of 60  $\mu$ m (Fig. 3C). Likewise, the dosage increased from 1.41  $\pm$  0.16 to  $13.88 \pm 0.14 \,\mu g$  as the length of Si NNs increased from 10 to 60  $\mu m$ at the fixed surface porosity of 30% (Fig. 3D).

For the loading of Bev to Si NNs, the Bev solution was diluted in an anhydrous (i.e.,  $\geq$ 99.9%) ethanol in a range of 1 to 20 µg ml<sup>-1</sup> to avoid unwanted dissolution of the tear-soluble contact lens. Figure 3E presents that there was no significant difference (n=5 for each group) in the total amount of Bev when diluted in a 5% (v/v) solution of ethanol diluent (blue bars) and standard phosphate-buffered saline (PBS) diluent at a pH of 7.4 (red bars) as compared to a non-diluted drug solution (black bars). In addition, the results of SDS-polyacrylamide gel electrophoresis (SDS-PAGE) in Fig. 3F show that the molecular weight of Bev diluted in anhydrous ethanol (four lanes on the right) was comparable to that of a nondiluted drug solution (second lane from the left) with a clear band at 150 kDa. In turn, there was no significant impact of the ethanol treatment on the in vitro stability of Bev.

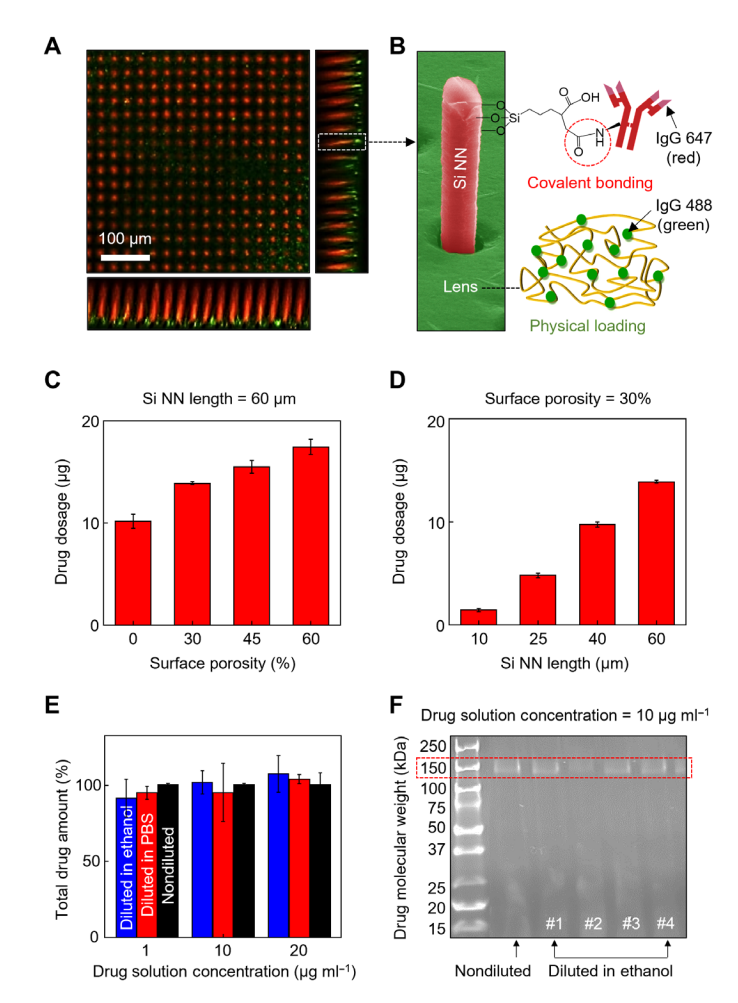


**Fig. 3. Drug loading mechanism and controls.** (**A**) Representative confocal fluorescence microscopy image of the covalently loaded IgG 647 (red) and physically loaded IgG 488 (green) on the surface of Si NNs and in the tear-soluble contact lens, respectively. (**B**) Colored SEM image of a Si NN with the schematic illustration of the drug loading mechanisms. (**C**) Drug dosage loaded on Si NNs as a function of surface porosity with the fixed length of  $60 \mu m$ . All data are represented as means  $\pm$  SD, with n = 3 for each group. (**D**) Drug dosage loaded on Si NNs as a function of length with the fixed surface porosity of 30%. All data are represented as means  $\pm$  SD, with n = 3 for each group. (**E**) Total drug amount when diluted in a 5% (v/v) solution of ethanol diluent (blue) and standard PBS diluent at the pH of 7.4 (red) as compared to a nondiluted solution (black). All data are represented as means  $\pm$  SD, with n = 3 for each group. (**F**) Representative results of SDS-PAGE revealing the molecular weight of Bev diluted in ethanol diluent (four lanes on the right) as compared to that of a nondiluted solution (second lane from the left).

# Dissolution profile and drug release kinetics

The intrinsic property of the tear-soluble contact lens in terms of bending stiffness (i.e., flexural rigidity) and dissolution rate was controlled to provide an optimal condition enabling both easy handling during lens fitting and rapid dissolution in tear fluid. Figure 4A presents the bending stiffness (red lines) and dissolution time (blue lines) of the tear-soluble contact lens when immersed in 5 ml of the simulated tear fluid at 37°C as a function of the lens thickness ranging from 4 to 80  $\mu$ m. For comparison, two different molecular weights of the tear-soluble contact lens, i.e., 31,000 (triangular symbols) and 61,000 (circular symbols), were tested. The

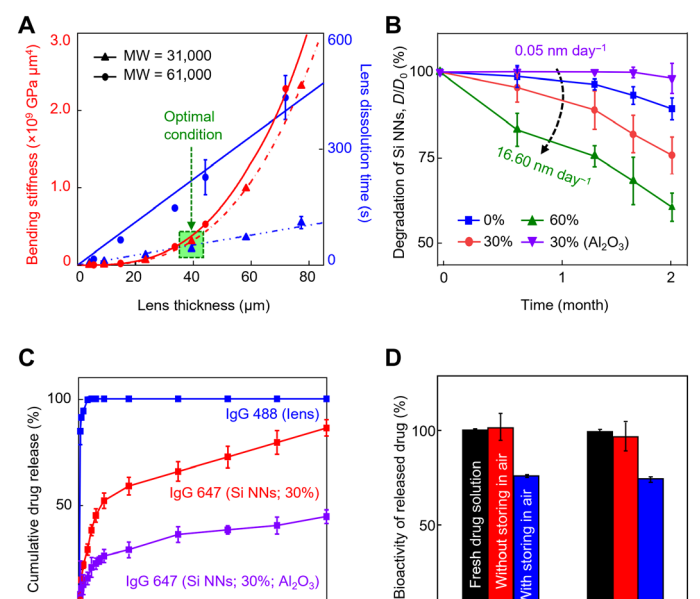


Fig. 4. Dissolution kinetics and drug release kinetics. (A) Measurement results of the bending stiffness (red lines) and dissolution time (blue lines) of the tearsoluble contact lens when immersed in 5 ml of the simulated tear fluid at 37°C as a function of the thickness ranging from 4 to 80 µm with molecular weights (MW) of 31,000 (triangular symbols) and 61,000 (circular symbols). All data are represented as means  $\pm$  SD, with n = 5 for each group. (B) Dissolution of Si NNs in a 1.4% (w/v) agarose gel containing 1 ml of the simulated tear fluid at 37°C for 2 months with varied surface porosity ranging from 0 to 60% and with the presence of a 3-nmthick pinhole-free Al<sub>2</sub>O<sub>3</sub> layer. All data are represented as means  $\pm$  SD, with n = 5 for each group. (C) Cumulative release of IgG 488 and 647 for 120 hours immersed in 1 ml of the simulated tear fluid at 37°C, each of which was physically and covalently loaded in the tear-soluble contact lens (blue line) and on the surface of Si NNs (i.e., porosity = 30%) with (red line) and without (purple line) the presence of the  $Al_2O_3$  passivation layer. All data are represented as means  $\pm$  SD, with n=3 for each group. (D) Results of ELISA to quantify the bioactivity of Bev at 12 and 120 hours of release from Si NNs after storage in a refrigerator at 4°C for 1 day (red bars) and 3 days (blue bars), as compared to a new vial of fresh Bev solution as a control (black bars). All data are represented as means  $\pm$  SD, with n = 3 for each group.

5.0

12

Drug release time (hour)

2.5

Time (day)

results show that the bending stiffness of the tear-soluble contact lens decreased to cubic of the lens thickness, while the dissolution rate decreased by more than fourfold (i.e., from 5.7 to 1.3  $\mu m \ s^{-1}$ ) as the molecular weight increased from 31,000 to 61,000. The green highlighted area in the graph indicates the empirically identified optimal condition using a 40- $\mu m$ -thick tear-soluble contact lens with the molecular weight of 31,000 at which both the bending stiffness (i.e., >3.07  $\times 10^8 \ GPa \ \mu m^4$ ) and dissolution rate (i.e., 5.7  $\mu m \ s^{-1}$ ) were sufficiently large to not only resist against bending, folding, and twisting (movie S1) but also get dissolved within a minute in the simulated tear fluid (movie S2).

Si NNs were also degraded within the cornea in the presence of tear fluid via hydrolysis reaction. The degradation rate of Si NNs was adjustable to control the drug release process within a prescribed time period. Figure 4B presents the gradual reduction of Si NNs in diameter  $(D/D_0)$  for 2 months while being embedded in a 1.4% (w/v) agarose gel containing 1 ml of the simulated tear fluid at 37°C to surrogate the human cornea. The simulated tear fluid was

refreshed every day to maintain the contents. For comparison, the surface porosity of Si NNs was varied from 0% (blue line) to 30% (red line) and to 60% (green line) by which the degradation of Si NNs was linearly accelerated from  $\sim 3.5$  to  $\sim 9.4$  and to  $\sim 16.6$  nm day<sup>-1</sup>, respectively. Furthermore, the degradation rate of Si NNs substantially decreased down to ~0.05 nm day<sup>-1</sup> (purple line) through the conformal passivation of a thin (i.e., 3-nm-thick) pinhole-free layer, such as aluminum oxide (Al<sub>2</sub>O<sub>3</sub>), across the surface (i.e., porosity = 30%) using an atomic layer deposition (ALD) (27). For instance, the Al<sub>2</sub>O<sub>3</sub>-passivated Si NNs exhibited at least five orders of magnitude prolonged degradation in tear fluid as compared to typical biodegradable composites, such as PLGA and MeHA (i.e., 24 to 120 μm day<sup>-1</sup>), that have been widely used for ocular drug delivery (8, 28). The corresponding SEM images of Si NNs while being degraded at a prescribed time interval are shown in fig. S8. Following the complete degradation of the Al<sub>2</sub>O<sub>3</sub> passivation layer in approximately 50 days, the degradation rate of Si NNs was gradually returned to normal (i.e., 3.9 to 7.8 nm day<sup>-1</sup>), as shown in fig. S9A. Metal oxide passivation layers, including Al<sub>2</sub>O<sub>3</sub>, have been often used to extend the lifetime of Si nanomaterials in biomedical applications with a high level of biocompatibility, biodegradability, and covalent drug immobilization (27, 29–31).

Figure 4C quantifies the biphasic release process of IgG 488 and 647 for 5 days when immersed in 1 ml of the simulated tear fluid at 37°C, each of which was physically and covalently loaded in the tear-soluble contact lens (blue line) and along the surface of Si NNs (i.e., porosity = 30%) without (red line) and with (purple line) the Al<sub>2</sub>O<sub>3</sub> passivation layer. The corresponding results for the complete release of IgG 488 and 647 up to 55 days are shown in fig. S9B. These results clearly display a biphasic release profile in which >85% of IgG 488 was quickly released from the tear-soluble contact lens within a minute (i.e., burst release) followed by the prolonged release of IgG 647 from Si NNs (i.e., long-term sustained release). The mean dissolution time (MDT), or drug-retaining ability, of  $T_{50\%}$ and  $T_{80\%}$  increased from 11 to 194 hours and from 96 to 814 hours with the presence of the Al<sub>2</sub>O<sub>3</sub> passivation layer, respectively. In turn, the Al<sub>2</sub>O<sub>3</sub>-passivated Si NNs exhibited substantially prolonged MDT in tear fluid as compared to typical biodegradable composites such as PLGA and MeHA (i.e.,  $T_{50\%} = 35$  to 48 hours and  $T_{80\%} = 75$ to 120 hours) that have been widely used in ocular drug delivery (8, 28).

Figure 4D presents the results of enzyme-linked immunosorbent assay (ELISA) to quantify the bioactivity of Bev at 12 and 120 hours of release from Si NNs after loading in anhydrous ethanol diluent (red bars) as compared to a new vial of fresh drug solution (i.e., Bev) as a control (black bars). The bioactivity of Bev remained barely changed in 120 hours after the loading without significant difference compared to the control (n = 3 for each group). On the other hand, nearly 25% of reduction in the bioactivity of Bev (i.e., denaturation) occurred in 3 days of storing in air after the loading due to oxidation (blue bars), which was also observed in previous studies (32, 33).

#### In vivo evaluation in a rabbit CNV model

To evaluate the therapeutic efficacy of Si NNs, a pilot study was conducted in a rabbit CNV model in vivo. CNV, or the invasion of new blood vessels into the avascular cornea, accounts for vision loss in 1.4 million people annually in the United States and is a potential consequence of various disorders such as dry eye syndrome, contact

lens use, corneal infections, surgery, trauma, and limbal stem cell deficiency (34). Vascular ingrowth into the cornea is also a major risk factor for rejection after corneal transplantation, and therefore, the treatment of CNV must be considered for visually impactful CNV or before corneal transplant (35). The current standard therapy for CNV involves the use of laser photocoagulation surgery or subconjunctival injection, but their efficacy is limited due to the protective corneal barriers and rapid nasolacrimal drainage (36). To address this critical need, Si NNs were applied to deliver an ocular drug (i.e., Bev) in treating rabbits with CNV with improved therapeutic efficacy and reduced side effects compared to current standard therapies.

A total of 27 New Zealand white rabbits (3 to 4 months old; 2.2 to 3.6 kg) were used in this study including both left and right eyes. The rabbit eye is similar to the human eye in terms of anatomical feature, phylogenesis, physiology, and pathophysiological response and has been extensively used as animal models for many eye diseases (21). For instance, the axial length (i.e., 18 mm), corneal thickness (540 to 560 µm), and curvature (8.3 to 9.0 mm in base curve radius) share many similarities to the human eye. In addition, a suture-induced rabbit CNV model has been well established to provide pathological similarity with human CNV (37). The animal procedures are as follows. First, a 7-0 silk suture was threaded through the peripheral cornea at approximately 1.5 mm away from the limbus of the rabbit eye. CNV was well developed at day 28 after suture placement (fig. S10A). The suture was then removed (fig. S10B). CNV was stabilized at day 7 after suture removal (fig. S10C). Next, the rabbit eye was treated with Si NNs by inserting the tearsoluble contact lens with gentle pressure using a cotton swab (movie S3). Thereafter, the tear-soluble contact lens was dissolved in tear fluid within less than a minute (fig. S11A). A few drops of artificial tear solution were applied to wash the rabbit eye. Last, the rabbit eye was monitored for 28 days using color and red-free photography as well as a custom-built optical coherence tomography (OCT) (fig. S11B) (38). For comparison, both the short (i.e., 10 µm) and long (i.e., 60 µm) Si NNs were tested after covalently loaded with a total of ~1.5 and ~14 μg of Bev, respectively. The results were also compared with control groups including (i) Si NNs without Bev, (ii) untreated rabbit eye, and (iii) subconjunctival injection (i.e., Bev without Si NNs). Details of the animal study protocol and group information are described in Materials and Methods.

Figure 5A shows a time series of the representative color, red-free, segmented, and overlay images of CNV at day 0 (i.e., pre-therapy) and days 1, 3, 7, 14, and 28 (i.e., on-therapy) using the 10-µm-long (left) and 60-µm-long (right) Si NNs with a fixed base diameter of 900 nm. The flowchart of the image processing is shown in fig. S12. Both groups of Si NNs showed great effect on treating CNV without noticeable difference between the groups. Notably, the minimum required amount of Bev (i.e., ~1.5 μg) using Si NNs was substantially lower than that of eye drops or subconjunctival injections (typically >1.2 mg) in the rabbit CNV model (39–41). Rapid reduction in CNV occurred from days 1 to 7, followed by sustained, persistent, and continued reduction up to day 28. Nearly complete removal of CNV appeared no later than day 28. No reduction in CNV occurred in the untreated group throughout the entire period, while the subconjunctival injection of Bev led to incomplete reduction in CNV (fig. S13). Figure 5B summarizes the results of vessel density (VD) analysis to quantify the dynamic change of CNV from days 0 to 28. The results show that the normalized VD reduced to nearly half

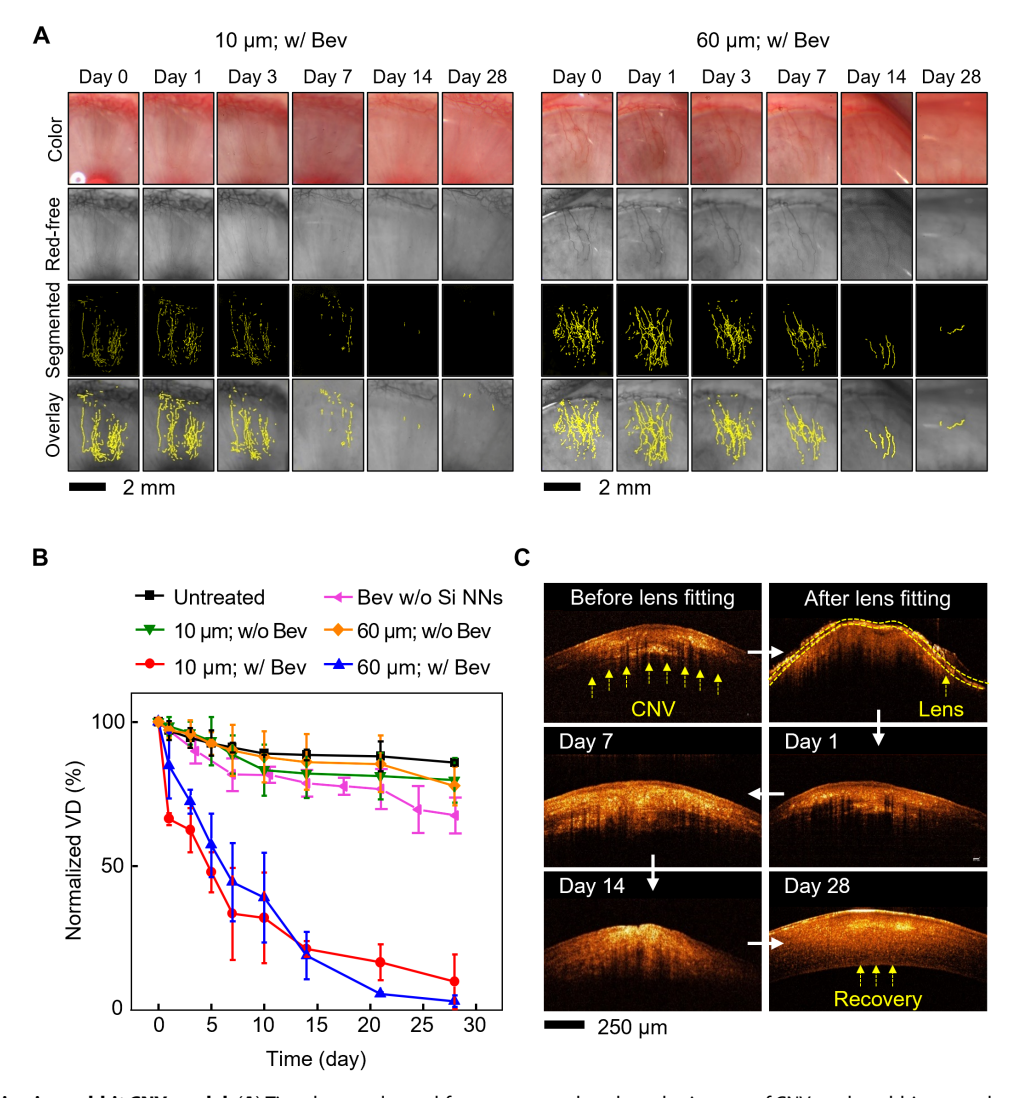


Fig. 5. In vivo evaluation in a rabbit CNV model. (A) Time-lapse color, red-free, segmented, and overlay images of CNV on the rabbit eye at day 0 (i.e., pre-therapy) and days 1, 3, 7, 14, and 28 (i.e., on-therapy) using 10-μm-long (left) and 60-μm-long (right) Si NNs. (B) Results of VD analysis to quantify the dynamic change of CNV from days 0 to 28. All data are represented as means  $\pm$  SD, with n = 3 for each group. (C) Time-lapse cross-sectional OCT images of the rabbit eye under therapy using the 60-μm-long Si NNs at day 0 (i.e., right before and after the lens fitting) and days 1, 7, 14, and 28 (i.e., on-therapy).

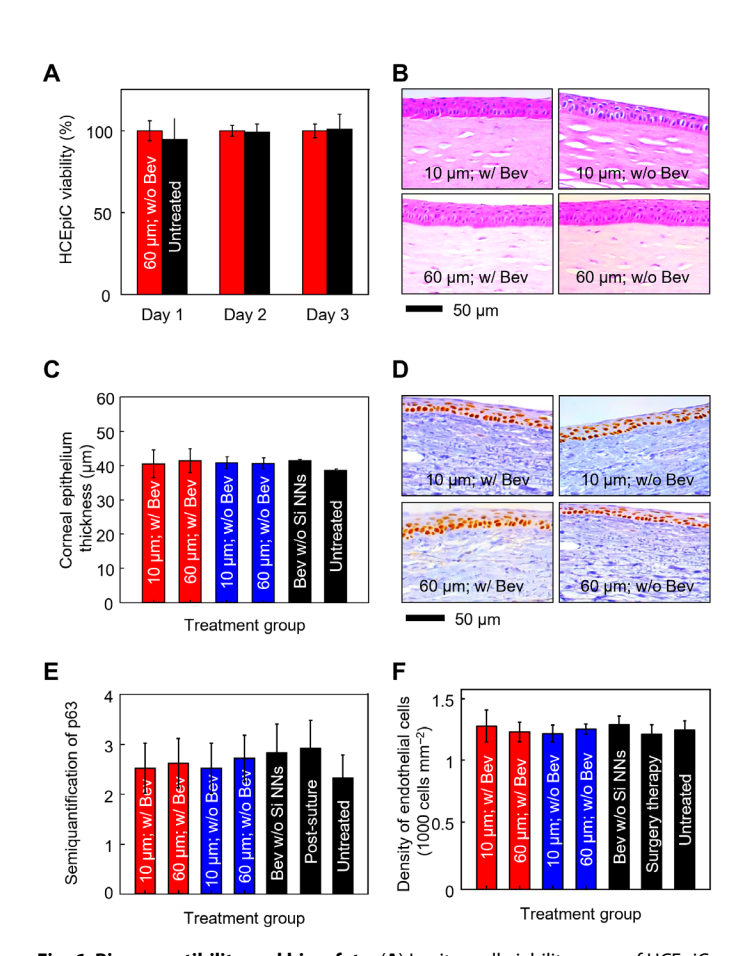
(i.e.,  $47.8\pm6.9\%$  for the  $10\mbox{-}\mu m\mbox{-}long$  Si NNs with Bev and  $57.2\pm11.1\%$  for the  $60\mbox{-}\mu m\mbox{-}long$  Si NNs with Bev) at day 5, followed by sustained, persistent, and continued reduction up to day 28 (i.e.,  $9.8\pm2.5\%$  for  $10\mbox{-}\mu m\mbox{-}long$  Si NNs with Bev and  $2.9\pm2.0\%$  for  $60\mbox{-}\mu m\mbox{-}long$  Si NNs with Bev). In the control groups, the normalized VD remained relatively unchanged over time (i.e.,  $79.7\pm7.7\%$  for the  $10\mbox{-}\mu m\mbox{-}long$  Si NNs without Bev,  $77.8\pm6.6\%$  for the  $60\mbox{-}\mu m\mbox{-}long$  Si NNs without Bev,  $81.1\pm2.5\%$  for the Bev without Si NNs, and  $85.8\pm0.9\%$  for the untreated group).

Figure 5C provides a time series of the cross-sectional OCT images of the rabbit eye under therapy using the 60-µm-long Si NNs at day 0 (i.e., right before and after the lens fitting) and days 1, 7, 14, and 28 (i.e., on-therapy). At day 0, the location of CNV (i.e., longitudinal shadows) and the tear-soluble contact lens was clearly visible in the OCT images as annotated with yellow dotted arrows and lines, respectively. Si NNs were invisible in the OCT images due to the nanoscale size (i.e., 900 nm in base diameter). Consistent with

previous observations, the rapid reduction of CNV occurred from days 1 to 7, followed by sustained, persistent, and continued reduction up to day 28. The OCT image at day 28 displays the normal structure of the cornea without any evidence of corneal damage, such as hemorrhage and corneal opacification, to confirm the recovery. The corresponding OCT images of the rabbit eye under therapy by the subconjunctival injection of Bev are shown in fig. S14, confirming the incomplete reduction of CNV on day 28. In close daily monitoring of the rabbits, no sign of discomfort was observed, including any change of orbital tightening, cheek flattening, nose shape, whisker position, and ear position, according to the established grimace scale (fig. S15A) (42). The ears were roughly perpendicular to the head, facing forward or to the side, held in an upright position away from the back and sides of the body with a more open and loosely curled shape, which indicates no pain. In addition, no reduction in the body weight of the rabbits was observed (fig. S15B).

#### **Biocompatibility and biosafety**

Time-dependent cytotoxicity of Si NNs to human corneal cell lines is an important consideration to reveal any adverse response at the cellular level (43). Figure 6A presents the in vitro cell viability assay of human corneal epithelial cells (HCEpiCs) that were seeded with (red bars) and without (black bars) the 60-µm-long Si NNs for 3 days using an MTT [3-(4,5-dimethylthiazol-2-yl)-2,5-diphenyltetrazolium bromide] assay kit (Sigma-Aldrich, USA). At the beginning of the cell culture process, the tear-soluble contact lens was quickly dissolved in the culture medium (EpiGRO Human Ocular Epithelia Complete Media, MilliporeSigma) at 37°C. Details of the entire cell culture process are described in Materials and Methods. The cell viability remained over 99% throughout the assay period without significant difference between the groups (n = 5 for each group). In



**Fig. 6. Biocompatibility and biosafety.** (**A**) In vitro cell viability assay of HCEpiCs that were seeded with (red bars) and without (black bars) the 60-μm-long Si NNs for 3 days. All data are represented as means  $\pm$  SD, with n=5 for each group. (**B**) Cross-sectional histological view of the rabbit cornea that was stained with both hematoxylin and eosin at day 28 on-therapy using the 10-μm-long (top) and 60-μm-long (bottom) Si NNs with (left) and without (right) the presence of Bev. (**C**) Measurement results of the corneal epithelium thicknesses. All data are represented as means  $\pm$  SD, with n=3 for each group. (**D**) Representative IHC results of the rabbit limbus that was stained with a p63 cell marker at day 28 on-therapy using the 10-μm-long (top) and 60-μm-long (bottom) Si NNs with (left) and without (right) the presence of Bev. (**E**) Semiquantification of the p63 cell marker. (**F**) Quantification of endothelial density. All data are represented as means  $\pm$  SD, with n=3 for each group.

turn, both Si NNs and the tear-soluble contact lens are expected to pose little risk for the development of corneal inflammation.

Figure 6B shows the cross-sectional histological view of the rabbit cornea that was stained with hematoxylin and eosin (H&E) at day 28 on-therapy using the 10-µm-long (top) and 60-µm-long (bottom) Si NNs with (left) and without (right) the presence of Bev. The corresponding view of the rabbit cornea in control groups is shown in fig. S16A. The corneal stroma remained normal without displaying any disorganization of corneal fibrils and collagen for all the groups. In addition, there was no significant difference in the corneal epithelium thickness among the groups (n = 3 for each group) (Fig. 6C). In turn, the ocular medication using Si NNs is expected to pose little risk for the development of corneal toxicity or other adverse reactions.

Figure 6D shows the representative immunohistochemistry (IHC) results of the rabbit limbus that was stained with a p63 cell marker at day 28 on-therapy using the 10-µm-long (top) and 60-µm-long (bottom) Si NNs with (left) and without (right) Bev. The corresponding IHC results of the rabbit limbus in control groups are shown in fig. S16B. The results show that the corneal limbus remained normal. The p63 expression remained nearly the same between the groups (n = 3 for each group) without statistical significance (Fig. 6E). The density of corneal endothelial cells remained also the same between the groups (n = 3 for each group) (Fig. 6F). No sign of change in the morphology of the corneal endothelial cells appeared in H&E images (fig. S17). In addition, the results of terminal deoxynucleotidyl transferase-mediated deoxyuridine triphosphate nick end labeling (TUNEL) assay also revealed no evidence of TUNEL-positive cells at day 28 after treatment (fig. S18). Together, Si NNs are expected to pose a minimal risk of inflammation or any toxic impact on the corneal endothelial cells and limbal stem cell function.

For comparison, the current standard surgical therapy, such as laser photocoagulation surgery, was also implemented in treating rabbits with CNV using a continuous-wave (CW) laser at 532 nm with pulse duration = 0.1 s, power = 450 mW, and width =  $75 \mu \text{m}$ . Numerous photocoagulation spots were noted in the cornea immediately (i.e., <1 min) after the laser photocoagulation surgery (fig. S19A). Circular scars were noted in the stroma and polymorphonuclear leukocytes, and inflammatory debris, while neovascularization was noted in a cleft between the corneal stromal lamellae (fig. S19B). A substantial reduction in the number of the limbal stem cells appeared at day 30 after surgery (fig. S19C). At day 7 after surgery, 64.7% of the CNV had recovered, while 21.4% of the CNV persisted until day 30 after surgery (fig. S19D). In turn, the laser photocoagulation surgery resulted in a less complete resolution of CNV as compared to the treatment using Si NNs while also causing damage to the surrounding corneal layers.

#### **DISCUSSION**

Our findings pave a new route toward minimally invasive, painless, and effective ocular drug delivery through the integration of controllably bioresorbable Si NNs with a tear-soluble contact lens. Si NNs provide optimal designs to penetrate and embed into the cornea in a minimally invasive manner and then undergo gradual degradation over the course of months. The prolonged degradation of Si NNs enables the long-term sustained release of therapeutic ocular drugs over typical bioresorbable composites. The tear-soluble contact

lens serves as a temporary holder for Si NNs during lens fitting and then completely dissolves in tear fluid within a minute, which helps preserve user comfort and clear vision without corneal stromal haze. In vivo evaluations of Si NNs in a rabbit CNV model support the therapeutic efficacy in treating a chronic ocular disease with reduced side effects beyond subconjunctival injection and surgical therapies. Si NNs can be potentially loaded with other ocular drugs to extend their applicability in treating a broad range of chronic ocular diseases such as glaucoma, melanoma, and cataract.

#### **MATERIALS AND METHODS**

#### Fabrication of Si NNs on Si wafer

The fabrication of Si NNs began by immersing a bulk Si wafer (p-type; 525 μm thick; 0 to 100 ohm·cm) in a buffered oxide etchant (J. T. Baker) for a minute to remove the native oxide layer. Standard photolithographic patterning and anisotropic deep reactive ion etching were performed to define a vertically ordered array of Si micropillars with a predefined aspect ratio. A thin passivation layer,  $(C_xF_y)_n$  polymer, was coated on the surface of the Si micropillars using octafluorocyclobutane (C<sub>4</sub>F<sub>8</sub>) gas at a flow rate of 130 sccm (standard cubic centimeters per minute) under a radio frequency (RF) plasma power of 800 W. The bottom roots of the Si micropillars were intentionally unpassivated wherein an anisotropic dry etching process was applied to form undercuts using sulfur hexafluoride (SF<sub>6</sub>) gas at a flow rate of 85 sccm under RF plasma power and platen power of 450 and 14 W, respectively. The remaining passivation layer on the surface of the Si micropillars was removed using an oxygen (O2) plasma (20 sccm; 150 W; 50 mtorr) for 15 min and piranha cleaning in a mixture solution containing 75% of sulfuric acid (H<sub>2</sub>SO<sub>4</sub>) and 25% of hydrogen peroxide (H<sub>2</sub>O<sub>2</sub>) by volume. The resulting Si micropillars were then immersed in a PBS (pH 7.4) at 67°C overnight and in 15% wt of potassium hydroxide (KOH) at 25°C for 10 min to shrink the overall size of the Si micropillars from microscale to nanoscale (i.e., Si NNs). The next step involved a metalassisted chemical etching (MACE) process in which Si NNs were immersed in a mixture solution containing 20 mM silver nitrate (AgNO<sub>3</sub>) and 49% of hydrofluoric acid solution to form nanopores along the surface of Si NNs. The overall surface porosity of Si NNs was controlled from 30 to 45 and to 60% by increasing the MACE time from 30 to 60 and to 90 s. Si NNs were then immersed in an Ag etchant solution (TFS, KI-I2 complex liquid, Transene) for a minute to remove the remaining Ag residues on the surface of Si NNs. A thin (i.e., 3-nm-thick) pinhole-free passivation layer such as Al<sub>2</sub>O<sub>3</sub> was deposited using ALD (Fiji, Cambridge Nanotechnology) with a precursor of trimethylaluminum at a pulse of 0.015 s. Here, the background pressure was set at 0.2 torr with nitrogen (N2) purge at 20 sccm for 20 s, while the substrate temperature was maintained at 150°C. Each cycle of this ALD process resulted in ~1-Å-thick Al<sub>2</sub>O<sub>3</sub> layer, which was repeated 30 times to form a total thickness of 3 nm. In this study, the base diameter, aspect ratio, and surface porosity of Si NNs were controlled in a range of 0.9 to 3  $\mu$ m, 3 to 66, and 0 to 60%, respectively. The drug loading capacity, dissolution rate, drug release profile, and therapeutic effects of Si NNs were compared.

#### Integration with tear-soluble contact lens

A 200-µm-thick PMMA film was spin-cast across the surface of the as-prepared Si NNs on a Si wafer and then annealed at 80°C for 2 hours. Here, approximately 16 µm of air gap was formed at the

bottom root of Si NNs due to surface tension. The PMMA film was then mechanically peeled off at a constant rate of 50 mm min<sup>-1</sup> using an automated peeling apparatus (Mark-10, Willrich Precision Instruments). PVA (500 µl) (2% wt, molecular weight = 31,000) was spin-casted across the exposed Si NNs and then cured in a vacuum chamber at 60°C for an hour. This step was repeated three times to form a 40-µm-thick PVA film. The entire structure was then trimmed into a circular shape (10 to 15 mm in diameter) using a biopsy punch (World Precision Instruments) and then pressed at ~ 20 kPa into a contact lens-shaped mold at 90°C for 5 min with the PMMA layer facing upward. The contact lens-shaped mold was pre-prepared through the molding of polydimethylsiloxane into several commercial artificial eyes. The resulting contact lens was then immersed in a bath of acetone at 70°C for 4 hours to selectively remove the PMMA layer, followed by rinsing with anhydrous ethanol. Last, a hole (2 to 8 mm in diameter) was punched at the pupil area using a biopsy punch (World Precision Instruments). For sterilization, the tear-soluble contact lens was immersed in a bath of anhydrous ethanol for 5 min and then exposed under ultraviolet (UV) light at 254 nm for 5 min before each use.

#### **Drug loading process**

Fluorescently labeled IgG 488 and 647 were used as surrogates of ocular drugs to optically visualize the drug release process. For the covalent bonding of IgG 647, 500  $\mu$ l of TESPSA was applied to Si NNs at room temperature for 10 min to functionalize the surface with silane and then washed with anhydrous ethanol. Specifically, 30  $\mu$ g of IgG 647 (Invitrogen) was prepared by mixing 50  $\mu$ l of IgG 647 with a concentration of 600  $\mu$ g ml<sup>-1</sup> and 950  $\mu$ l of anhydrous ethanol. In this solution, Si NNs were immersed for 30 min at room temperature, followed by rinsing with anhydrous ethanol. The covalent bonding mechanism for Bev was identical to that for IgG 647. For the physical loading of IgG 488, 10  $\mu$ l of IgG 488 (Invitrogen) with a concentration of 100  $\mu$ g ml<sup>-1</sup> was mixed with 1.5 ml of PVA (2% wt; molecular weight = 31,000; Mowiol 4-88, Sigma-Aldrich) and stirred at 300 rpm for a minute.

#### **Drug release monitoring**

The total amount of IgG 488 and 647 was obtained by measuring the fluorescent intensity of the solution with a plate reader (Synergy Neo plate reader, BioTek Instruments) at the excitation and emission of 594 and 665 nm, respectively. The measured total amount of IgG 647 was subtracted from the applied dosage of 30 μg, resulting in the loaded drug dosage. The release profiles were obtained by placing the tear-soluble contact lens on a cell strainer (pluriStrainer, pluriSelect) and then immersing it into 4 ml of the simulated tear at 37°C. The cell strainer was used to prevent cross-talk in fluorescent signals from the free-floating Si NNs in the solution after the complete dissolution of the tear-soluble contact lens. At predetermined intervals, the released solution was withdrawn and replenished with the fresh simulated tear. The drug concentration was calculated by measuring the fluorescent intensity with a plate reader (Synergy Neo plate reader, BioTek Instruments) at the excitation and emission of 594/665 nm and 488/525 nm, respectively. Solutions with known concentration were measured to generate standard curves.

#### Simulated tear fluid

For the preparation of the simulated tear fluid, 100 ml of deionized water was mixed with 0.68 g of sodium chloride (NaCl), 0.22 g of

sodium bicarbonate (NaHCO<sub>3</sub>), 0.008 g of calcium chloride dihydrate (CaCl<sub>2</sub>·2H<sub>2</sub>O), and 0.14 g of potassium chloride (KCl). All chemicals were obtained from Sigma-Aldrich.

#### **Optical transmittance measurements**

The optical transmittance of the tear-soluble contact lens was measured using a UV-visible spectrophotometer (Lambda950, Perkin-Elmer) at wavelengths of 300 to 800 nm. For comparison, the optical transmittance of a commercial soft contact lens (Frequency 55 Aspheric; CooperVision) was also measured.

#### **Optical haze analysis**

The optical haze of the tear-soluble contact lens was analyzed by measuring total and diffuse transmission using a fiber bundle-coupled spectrometer (VS140 VIS-NIR, Horiba Jobin Yvon) equipped with an integrating sphere (IS210C, Thorlabs). A Xenon lamp was used as a light source. For comparison, the optical haze of a commercial soft contact lens (Frequency 55 Aspheric, CooperVision) was also examined. The haze is defined by the ratio of the diffuse transmission relative to the total transmission.

# In vitro stability of Bev

For the evaluation of the in vitro drug stability, the drug solution (i.e., Bev) with a concentration of 1, 10, and 20 µg ml<sup>-1</sup> was prepared by diluting in a 5% (v/v) solution of ethanol diluent and PBS. Bicinchoninic acid (BCA) assay was performed with the MicroBCA Protein Assay Kit (Thermo Fisher Scientific) for the measurement of the total amount of Bev in each solution, where 150 µl of each solution was mixed with 150 µl of working reagent, followed by incubation for 30 min at 37°C in 96-well plates. Absorbance was measured at 562 nm with a plate reader (Synergy Neo plate reader, BioTek Instruments). The measurement data were expressed as averages ± SD. The SDS-PAGE was performed by comparing the ethanoldiluted Bev with the fixed concentration of 10 µg ml<sup>-1</sup> as compared to the nondiluted solution. A 5-µl Precision Plus Protein Kaleidoscope Standards (Bio-Rad) was loaded on the first lane from the left as a reference with 15  $\mu$ l of the nondiluted and ethanol-diluted Bev on the second and third to sixth lane from the left, respectively. Electrophoresis was performed with 15 µl of 4 to 20% well Mini-Protean TGX Gels (Bio-Rad), a tris/glycine buffer (Bio-Rad) as a running buffer, 4.75 µl of Laemmli sample buffer (Bio-Rad) mixed with 0.25 µl of β-mercaptoethanol (Sigma-Aldrich) as loading buffer, and GelCode Blue Safe Protein Stain (Thermo Fisher Scientific) for staining. Electrophoresis was performed at 100 V for 90 min and imaged with Azure 600 (Azure Biosystems).

#### **Bioactivity of Bev**

Si NNs were prepared by loading 1  $\mu g$  of Bev and then immersed in 1 ml of the simulated tear at 37°C. For comparison, a control group of Si NNs with Bev was stored at 4°C for 3 days. At 12 and 120 hours of release, the simulated tear was extracted for bioactivity measurement. Anti-Bev antibody HCA182 (Bio-Rad) was used as a capture antibody along with HCA184 (Bio-Rad) as a detection reagent. HCA182 (100  $\mu$ l) at 1  $\mu g$  ml<sup>-1</sup> in PBS was coated overnight at 4°C on 98-well MaxiSorp black plates (Thermo Fisher Scientific) and treated with 300  $\mu$ l of 5% cow serum albumin (Thermo Fisher Scientific) in PBS. Tween 20 (0.05%) (PBST) was added as a blocking agent. Both the freshly prepared Bev from 0.1 to 1000 ng ml<sup>-1</sup> in 10% human serum (Sigma-Aldrich) in PBST and the released Bev from Si NNs

were added to the well. HCA184P (100  $\mu$ l) at 4  $\mu$ g ml $^{-1}$  in HISPEC buffer (Bio-Rad) was loaded to each well, followed by adding 100  $\mu$ l of QuantaBlu (Thermo Fisher Scientific). Fluorescent signals were measured with a plate reader (Synergy Neo plate reader, BioTek Instruments) at the excitation and emission at 325 and 420 nm, respectively. The measured data were expressed as averages  $\pm$  SD.

#### In vitro cell viability assay

The tear-soluble contact lens, with no drug loaded, was placed into a 24-well plate. HCEpiCs (MilliporeSigma) were seeded inside the wells with a density of  $1\times10^5$  per well in 1 ml of cell medium (EpiGRO Human Ocular Epithelia Complete Media, MilliporeSigma) and then incubated at 37°C with 5% carbon dioxide (CO<sub>2</sub>) for 3 days. At the beginning of the cell culture process, the tear-soluble contact lens was quickly dissolved in the culture medium. At each day, a 3-(4,5-dime-thylthiazol-2-yl)-2,5-diphenyltetrazolium bromide (MilliporeSigma) reagent was added and incubated for 3 hours. Following the removal of the cell medium, the cells were lysed with dimethyl sulfoxide (Thermo Fisher Scientific). The absorbance of each well was measured with a microplate reader (Synergy NEO, BioTek) at 575 nm. The measurement data were expressed as averages  $\pm$  SD.

#### In vivo rabbit study

All the in vivo studies in rabbits were implemented in accordance with the instruction of the Association for Research in Vision and Ophthalmology (ARVO) statement on the care and use of laboratory animals in Ophthalmic and Vision Research. The protocol for animal experiments was approved by the University Institutional Animal Care and Use Committee (IACUC) (protocol number PRO00008566). In this study, the number of rabbits was determined based on a power calculation for statistical significance while minimizing the number of rabbits to be sacrificed with a minimum of two to three rabbits in each treatment group. The rabbit vitals such as mucous membrane color, body temperature, heart rate, and respiratory rate were examined and recorded as a general procedure using a pulse oximeter (Smiths Medical). The rabbit pupils were dilated with 1% tropicamide ophthalmic and 2.5% phenylephrine hydrochloride ophthalmic. The rabbits were anesthetized through the intramuscular injection of ketamine (40 mg kg<sup>-1</sup>, 100 mg ml<sup>-1</sup>; Ketalar, Par Pharmaceutical) and xylazine (5 mg kg<sup>-1</sup>, 100 mg ml<sup>-1</sup>; Anased; MWI Veterinary Supply, VetOne, Boise). To keep the rabbits fully anesthetized throughout the entire period of experiments, a vaporized isoflurane anesthetic was applied to provide oxygen (1000 ml min<sup>-1</sup>) and isoflurane (0.75%; Surgivet). Before performing experiments, a drop of 0.5% topical proparacaine (Alcaine, Alcon) was applied onto the eye for topical anesthesia. In addition, a few drops of artificial tear solution (Systane, Alcon) were provided regularly to prevent dehydration of the cornea. A water-circulating blanket (TP-700, Stryker Corporation) was used to maintain the temperature of the rabbits. The rabbits were humanely euthanized by intravenous injection of a euthanasia solution (0.22 mg kg<sup>-1</sup>; Beuthanasia-D Special, Intervet) through the marginal ear vein.

## In vivo CNV model preparation

A total of 24 New Zealand white rabbits were tested for in vivo CNV model including both left and right eyes. The CNV model was implemented as follows. First, a 7-0 silk suture was placed through the peripheral cornea at approximately 1.5 mm away from the limbus

of the rabbit eye. During the suture procedure, the animals were observed under an operating microscope to ensure that the suture was placed radially to the limbus and to avoid the suture penetrating deeper than approximately half the corneal thickness. Corneal angiogenesis was monitored by photography and red-free imaging. At day 28 after suture, the suture was removed and monitored for another week during CNV stabilization. At day 7 after suture removal, the CNV therapy was applied to the rabbits. The following eight groups were tested: (i) untreated healthy cornea (control), (ii) CNV without therapy, (iii) CNV treated by subconjunctival injection of Bev, (iv) CNV treated using the 10-µm-long Si NNs without Bev, (v) CNV treated using the 10-μm-long Si NNs with Bev, (vi) CNV treated using the 60-µm-long Si NNs without Bev, (vii) CNV treated using 60-µm-long Si NNs with Bev, and (viii) CNV treated with laser photocoagulation surgery. In this in vivo study, no synergistic effect was expected from biphasic drug release because Si NNs induced no noticeable inflammation or any toxic sign in the rabbit eyes. Therefore, no anti-inflammatory drugs or other ocular drugs were embedded in the tear-soluble contact lens. The CNV was monitored using photography, red-free photography, and OCT imaging at days 1, 3, 5, 7, 14, 21, and 28. The corneal thickness and composition were evaluated using a cross-sectional B-scan OCT and confirmed using H&E staining imaging. All CNV model rabbits were imaged before and after 5-min post-therapy and followed for up to a month.

#### Color and red-free photography

A custom-modified 50° color photography system (Topcon 50EX, Topcon Corporation) was used to visualize the CNV network. Photographs of CNV were captured using an Electro-Optical System (EOS) five-dimensional camera with a resolution of  $5472 \times 3648$ pixels at the single pixel size of 6.55 μm<sup>2</sup>. Red-free photography images were implemented on the same Topcon 50EX camera using appropriate internal excitation and emission filters. In addition, the picture style was changed to monochrome for the enhanced visualization of new blood vessels. The red-free image offered high signal contrast of newly developed blood vessels, suitable for quantifying the dynamic change in CNV over time.

#### In vivo OCT

The CNV pre- and post-therapy was monitored using a custombuilt spectral domain OCT imaging system (Ganymede-II-HR, Thorlabs). To use it in rabbit eyes, an ocular lens was added after the scan lens to allow light to focus on the retina. A dispersion compensation glass was added in the reference arm. Two super-luminescent diodes were used in the OCT imaging system with center wavelengths of 846 and 932 nm for the light sources to excite the tissues. Back-scattered light from the tissues was captured and reconstructed for OCT images. The lateral and axial resolutions were estimated to be 3.8 and 4.0 µm in air, respectively.

## Image segmentation and VD analysis

To quantify the dynamic change in CNV vessels after therapy, the VD was determined at different time points. The treated regions were manually selected using a crop function in MATLAB (MathWorks). Then, the image contrast of the cropped image was enhanced using an adaptive histogram equalization function. Edge detection function was applied to segment the boundary of the CNV vessels. The VD was determined by counting each pixel along with the segmented

CNV vessels. The relative VD at each time point was determined by normalizing the VD post-therapy to the VD pre-therapy as the following formula (37)

$$\%VD = \frac{VD \text{ at the time post-therapy}}{VD \text{ pre-therapy}} \times 100$$
 (1)

#### In vivo biosafety evaluation

To ensure the in vivo biosafety of Si NNs to the cornea, evaluations were performed on the corneal endothelium, epithelium, limbal stem cells, and stromal integrity. The body weight of the rabbits was also accessed daily on-therapy and post-therapy for up to a month in each group. To evaluate microstructural change of the treated tissue, H&E, TUNEL, and IHC staining were conducted. After euthanasia, the rabbit eye was isolated and fixed in a 10% neutral buffered formalin (VWR). The cornea and limbus were extracted and embedded in a paraffin. Then, the paraffin-embedded tissues were sectioned to a thickness of 4 µm using the Leica Autostainer XL (Leica Biosystems) and stained with 1:400 of H&E, TUNEL DeadEnd Kits, and anti-p63 antibody (Invitrogen). To evaluate the potential effect of Si NNs on the function and proliferation of corneal endothelium cells, the density of endothelium cells was quantified. The corneal tissues were positioned on endothelial side up and sectioned along horizontal directions. The specimens were stained with H&E, and the number of endothelial cells was counted using the Imaris 9.1.0 imaging analysis software (Bitplane AG). At least a dozen of H&E images was obtained at 40× and used to evaluate endothelial cells. The sections were observed using the Leica DM600 light microscope (Leica Biosystems). The H&E, TUNEL, and IHC images were acquired using the BF450C camera (DM600, Leica Biosystems). To evaluate the potential effect of Si NNs on the function and proliferation of limbal stem cells, protein expression was quantified using semiquantitative analysis on IHC images. The high-power field (HPF) at ×40 magnification was used for each group. The percentage of p63-positive cells per HPF was determined and scored by the following reference scales: 0% (score 0) 1 to 33% scored by the following reference scales: 0% (score 0), 1 to 33% (score 1), 34 to 67% (score 2), 68 to 99% (score 3), and 100% (score 4). The rabbits were monitored daily on-therapy on a pain or grimace scale, which has been well established and validated (42). Facial expressions were evaluated to identify any discomfort, including any change of orbital tightening, cheek flattening, nose shape, whisker position, and ear position. In addition, the rabbits were evaluated for any sign of discomfort, including reduced food and/or water intake, reduced activity, or decreased interaction with environment, restlessness or frequent alteration in posture, hunched posture, or tensing of musculature, increased or abnormal aggression, scratching/ licking at painful area, failure to groom, increased salivation, teeth grinding, and increased respiratory rate.

# **TUNEL** assay

The TUNEL assay was implemented using the Cell Death Detection Kit (Sigma-Aldrich) to detect apoptotic markers on treated tissues. The paraffin-embedded tissues were deparaffinized using xylene and ethanol at the concentration of 50, 70, 85, 95, and 100% and then washed with PBS three times for each step. Apoptosis detection process was followed under the guideline of BD DeadEnd detection kits. The resulting specimens were mounted with ProLong Gold Antifade Mountant with DAPI (4',6-diamidino-2-phenylindole; P36931, Invitrogen). Images were acquired using a fluorescence microscope

(DM6000, Leica). Green fluorescence indicates the location of apoptotic tissue stained by fluorescein isothiocyanate (FITC), and blue fluorescence shows the detected DAPI-stained nuclei.

#### Subconjunctival injection

Subconjunctival injection of anti-VEGF Bev was conducted as a positive control group. One hundred microliters of Bev (2.5 mg ml<sup>-1</sup>) was administered into the subconjunctival space using a 30-gauge needle. The injection location was carried out at a distance of 3.5 to 4 mm from the corneal limbus and adjacent to the pathological blood vessel area, leading to the formation of conjunctival bullae (fig. S20). Color, red-free, and OCT examinations were performed at baseline and 1, 3, 7, 14, and 28 days.

#### Laser photocoagulation surgery

For comparison, the current standard therapy, such as laser photocoagulation surgery, was implemented (37). A total of six rabbits were treated by applying a CW laser with pulse duration = 0.1 s, power = 450 mW, and laser spot size = 75  $\mu m$  using the VITRA 532 nm Photocoagulator (Quantel Medical) equipped with a Zeiss SL130 Slit lamp adapter. Laser spots were applied sequentially along the vessel path. No overlap between each laser spot was observed.

#### Statistical analyses

Statistical analyses were carried out using OriginPro 2021 software. One-way analysis of variance (ANOVA) analysis with Tukey test with significance at the 0.001 level was used for Figs. 3E, 4D, and 6, A, C, and F.

#### **SUPPLEMENTARY MATERIALS**

Supplementary material for this article is available at https://science.org/doi/10.1126/sciadv.abn1772

#### **REFERENCES AND NOTES**

- K. Zhang, L. Zhang, R. N. Weinreb, Ophthalmic drug discovery: Novel targets and mechanisms for retinal diseases and glaucoma. *Nat. Rev. Drug Discov.* 11, 541–559 (2012)
- 2. A. F. Clark, T. Yorio, Ophthalmic drug discovery. Nat. Rev. Drug Discov. 2, 448–459 (2003).
- R. Ganugula, M. Arora, M. A. Lepiz, Y. Niu, B. K. Mallick, S. C. Pflugfelder, E. M. Scott, M. N. V. Ravi Kumar, Systemic anti-inflammatory therapy aided by double-headed nanoparticles in a canine model of acute intraocular inflammation. *Sci. Adv.* 6, 1–11 (2020).
- J. G. Ghosh, A. A. Nguyen, C. E. Bigelow, S. Poor, Y. Qiu, N. Rangaswamy, R. Ornberg, B. Jackson, H. Mak, T. Ezell, V. Kenanova, E. de La Cruz, A. Carrion, B. Etemad-Gilbertson, R. G. Caro, K. Zhu, V. George, J. Bai, R. Sharma-Nahar, S. Shen, Y. Wang, K. K. Subramanian, E. Fassbender, M. Maker, S. Hanks, J. Vrouvlianis, B. Leehy, D. Long, M. Prentiss, V. Kansara, B. Jaffee, T. P. Dryja, M. Roguska, Long-acting protein drugs for the treatment of ocular diseases. Nat. Commun. 8. 14837 (2017).
- X. Yuan, D. C. Marcano, C. S. Shin, X. Hua, L. C. Isenhart, S. C. Pflugfelder, G. Acharya, Ocular drug delivery nanowafer with enhanced therapeutic efficacy. ACS Nano 9, 1749–1758 (2015).
- J. H. Jung, B. Chiang, H. E. Grossniklaus, M. R. Prausnitz, Ocular drug delivery targeted by iontophoresis in the suprachoroidal space using a microneedle. J. Control. Release 277, 14–22 (2018).
- R. Jamaledin, C. K. Y. Yiu, E. N. Zare, L. N. Niu, R. Vecchione, G. Chen, Z. Gu, F. R. Tay, P. Makvandi, Advances in antimicrobial microneedle patches for combating infections. Adv. Mater. 32, 2002129 (2020).
- A. Than, C. Liu, H. Chang, P. K. Duong, C. M. G. Cheung, C. Xu, X. Wang, P. Chen, Self-implantable double-layered micro-drug-reservoirs for efficient and controlled ocular drug delivery. *Nat. Commun.* 9, 4433 (2018).
- K. T. M. Tran, T. D. Gavitt, N. J. Farrell, E. J. Curry, A. B. Mara, A. Patel, L. Brown, S. Kilpatrick, R. Piotrowska, N. Mishra, S. M. Szczepanek, T. D. Nguyen, Transdermal microneedles for the programmable burst release of multiple vaccine payloads. *Nat. Biomed. Eng.* 5, 998–1007 (2020).

- W. Li, R. N. Terry, J. Tang, M. R. Feng, S. P. Schwendeman, M. R. Prausnitz, Rapidly separable microneedle patch for the sustained release of a contraceptive. *Nat. Biomed. Eng.* 3, 220–229 (2019).
- Y. Lee, T. Kang, H. R. Cho, G. J. Lee, O. K. Park, S. Kim, B. Lee, H. M. Kim, G. D. Cha, Y. Shin, W. Lee, M. Kim, H. Kim, Y. M. Song, S. H. Choi, T. Hyeon, D. Kim, Localized delivery of theranostic nanoparticles and high-energy photons using microneedles-onbioelectronics. *Adv. Mater.* 33, 2100425 (2021).
- C. Chiappini, Y. Chen, S. Aslanoglou, A. Mariano, V. Mollo, H. Mu, E. de Rosa, G. He, E. Tasciotti, X. Xie, F. Santoro, W. Zhao, N. H. Voelcker, R. Elnathan, Tutorial: Using nanoneedles for intracellular delivery. *Nat. Protoc.* 16, 4539–4563 (2021).
- S. Gopal, C. Chiappini, J. Penders, V. Leonardo, H. Seong, S. Rothery, Y. Korchev, A. Shevchuk, M. M. Stevens, Porous silicon nanoneedles modulate endocytosis to deliver biological payloads. *Adv. Mater.* 31, 1806788 (2019).
- C. Chiappini, E. de Rosa, J. O. Martinez, X. Liu, J. Steele, M. M. Stevens, E. Tasciotti, Biodegradable silicon nanoneedles delivering nucleic acids intracellularly induce localized in vivo neovascularization. *Nat. Mater.* 14, 532–539 (2015).
- S. Mitragotri, D. G. Anderson, X. Chen, E. K. Chow, D. Ho, A. Kabanov, J. M. Karp, K. Kataoka, C. A. Mirkin, S. H. Petrosko, J. Shi, M. M. Stevens, S. Sun, S. Teoh, S. S. Venkatraman, Y. Xia, S. Wang, Z. Gu, C. Xu, Accelerating the translation of nanomaterials in biomedicine. ACS Nano 9, 6644–6654 (2015).
- H. Kim, H. Jang, B. Kim, M. K. Kim, D. S. Wie, H. S. Lee, D. R. Kim, C. H. Lee, Flexible elastomer patch with vertical silicon nanoneedles for intracellular and intratissue nanoinjection of biomolecules. Sci. Adv. 4. eaau6972 (2018).
- S. Basu, A. J. Hertsenberg, M. L. Funderburgh, M. K. Burrow, M. M. Mann, Y. Du, K. L. Lathrop, F. N. Syed-Picard, S. M. Adams, D. E. Birk, J. L. Funderburgh, Human limbal biopsy-derived stromal stem cells prevent corneal scarring. Sci. Transl. Med. 6, 266ra172 (2014).
- S.-K. Kang, R. K. J. Murphy, S.-W. Hwang, S. M. Lee, D. V. Harburg, N. A. Krueger, J. Shin, P. Gamble, H. Cheng, S. Yu, Z. Liu, J. G. McCall, M. Stephen, H. Ying, J. Kim, G. Park, R. C. Webb, C. H. Lee, S. Chung, D. S. Wie, A. D. Gujar, B. Vemulapalli, A. H. Kim, K. M. Lee, J. Cheng, Y. Huang, S. H. Lee, P. V. Braun, W. Z. Ray, J. A. Rogers, Bioresorbable silicon electronic sensors for the brain. *Nature* 530, 71–76 (2016).
- L. Yin, A. B. Farimani, K. Min, N. Vishal, J. Lam, Y. K. Lee, N. R. Aluru, J. A. Rogers, Mechanisms for hydrolysis of silicon nanomembranes as used in bioresorbable electronics. Adv. Mater. 27, 1857–1864 (2015).
- S. W. Hwang, H. Tao, D. H. Kim, H. Cheng, J. K. Song, E. Rill, M. A. Brenckle, B. Panilaitis, S. M. Won, Y. S. Kim, Y. M. Song, K. J. Yu, A. A. Ameen, R. Li, Y. Su, M. Yang, D. L. Kaplan, M. R. Zakin, M. J. Slepian, Y. Huang, F. G. Omenetto, J. A. Rogers, A physically transient form of silicon electronics. *Science* 337, 1640–1644 (2012).
- E. M. del Amo, A. Urtti, Rabbit as an animal model for intravitreal pharmacokinetics:
   Clinical predictability and quality of the published data. Exp. Eye Res. 137, 111–124 (2015).
- Y. C. Kim, M. D. Shin, S. F. Hackett, H. T. Hsueh, R. L. e Silva, A. Date, H. Han, B. J. Kim, A. Xiao, Y. Kim, L. Ogunnaike, N. M. Anders, A. Hemingway, P. He, A. S. Jun, P. J. McDonnell, C. Eberhart, I. Pitha, D. J. Zack, P. A. Campochiaro, J. Hanes, L. M. Ensign, Gelling hypotonic polymer solution for extended topical drug delivery to the eye. *Nat. Biomed. Eng.* 4, 1053–1062 (2020).
- I. Seah, X. J. Loh, X. Su, A topical gel for extended ocular drug release. Nat. Biomed. Eng. 4, 1024–1025 (2020).
- P. L. Destruel, N. Zeng, M. Maury, N. Mignet, V. Boudy, In vitro and in vivo evaluation
  of in situ gelling systems for sustained topical ophthalmic delivery: State of the art
  and beyond. *Drug Discov. Today* 22, 638–651 (2017).
- N. Ferrara, A. P. Adamis, Ten years of anti-vascular endothelial growth factor therapy. Nat. Rev. Drug Discov. 15, 385–403 (2016).
- H. Kim, H. S. Lee, Y. Jeon, W. Park, Y. Zhang, B. Kim, H. Jang, B. Xu, Y. Yeo, D. R. Kim, C. H. Lee, Bioresorbable, miniaturized porous silicon needles on a flexible water-soluble backing for unobtrusive, sustained delivery of chemotherapy. ACS Nano 14, 7227–7236 (2020)
- W. Zhou, X. Dai, T.-M. M. Fu, C. Xie, J. Liu, C. M. Lieber, Long term stability of nanowire nanoelectronics in physiological environments. *Nano Lett.* 14, 1614–1619 (2014).
- 28. Y. Lee, S. Park, S. il Kim, K. Lee, W. Ryu, Rapidly detachable microneedles using porous water-soluble layer for ocular drug delivery. *Adv. Mater. Technol.* 5, 1901145 (2020).
- W. Bai, J. Shin, R. Fu, I. Kandela, D. Lu, X. Ni, Y. Park, Z. Liu, T. Hang, D. Wu, Y. Liu, C. R. Haney, I. Stepien, Q. Yang, J. Zhao, K. R. Nandoliya, H. Zhang, X. Sheng, L. Yin, K. MacRenaris, A. Brikha, F. Aird, M. Pezhouh, J. Hornick, W. Zhou, J. A. Rogers, Bioresorbable photonic devices for the spectroscopic characterization of physiological status and neural activity. *Nat. Biomed. Eng.* 3, 644–654 (2019).
- J. Shin, Y. Yan, W. Bai, Y. Xue, P. Gamble, L. Tian, I. Kandela, C. R. Haney, W. Spees, Y. Lee, M. Choi, J. Ko, H. Ryu, J.-K. Chang, M. Pezhouh, S.-K. Kang, S. M. Won, K. J. Yu, J. Zhao, Y. K. Lee, M. R. MacEwan, S.-K. Song, Y. Huang, W. Z. Ray, J. A. Rogers, Bioresorbable pressure sensors protected with thermally grown silicon dioxide for the monitoring of chronic diseases and healing processes. *Nat. Biomed. Eng.* 3, 37–46 (2018).

# SCIENCE ADVANCES | RESEARCH ARTICLE

- H. Fang, K. J. Yu, C. Gloschat, Z. Yang, E. Song, C.-H. Chiang, J. Zhao, S. M. Won, S. Xu, M. Trumpis, Y. Zhong, S. W. Han, Y. Xue, D. Xu, S. W. Choi, G. Cauwenberghs, M. Kay, Y. Huang, J. Viventi, I. R. Efimov, J. A. Rogers, Capacitively coupled arrays of multiplexed flexible silicon transistors for long-term cardiac electrophysiology. *Nat. Biomed. Eng.* 1, 1–12 (2017)
- C. Nowak, J. K. Cheung, S. M. Dellatore, A. Katiyar, R. Bhat, J. Sun, G. Ponniah, A. Neill, B. Mason, A. Beck, H. Liu, Forced degradation of recombinant monoclonal antibodies: A practical guide. MAbs 9, 1217–1230 (2017).
- H. Yamazoe, Antibody immobilization technique using protein film for high stability and orientation control of the immobilized antibody. *Mater. Sci. Eng. C* 100, 209–214 (2019)
- J. H. Chang, N. K. Garg, E. Lunde, K. Y. Han, S. Jain, D. T. Azar, Corneal neovascularization: An anti-VEGF therapy review. Surv. Ophthalmol. 57, 415–429 (2012).
- O. Azevedo Magalhaes, A. Shalaby Bardan, M. Zarei-Ghanavati, C. Liu, Literature review and suggested protocol for prevention and treatment of corneal graft rejection. Eye 34, 442–450 (2020).
- S. Feizi, A. A. Azari, S. Safapour, Therapeutic approaches for corneal neovascularization. Eve Vision 4. 1–10 (2017).
- Y. Qin, Y. Yu, J. Fu, X. Xie, T. Wang, M. A. Woodward, Y. M. Paulus, X. Yang, X. Wang, Photo-mediated ultrasound therapy for the treatment of corneal neovascularization in rabbit eyes. *Transl. Vis. Sci. Technol.* 9, 16 (2020).
- V. P. Nguyen, W. Qian, Y. Li, B. Liu, M. Aaberg, J. Henry, W. Zhang, X. Wang, Y. M. Paulus, Chain-like gold nanoparticle clusters for multimodal photoacoustic microscopy and optical coherence tomography enhanced molecular imaging. *Nat. Commun.* 12, 1–14 (2021).
- Y. C. Kim, H. F. Edelhauser, M. R. Prausnitz, Targeted delivery of antiglaucoma drugs to the supraciliary space using microneedles. *Invest. Ophthalmol. Vis. Sci.* 55, 7387–7397 (2014).
- S. J. Bakri, M. R. Snyder, J. M. Reid, J. S. Pulido, R. J. Singh, Pharmacokinetics of intravitreal bevacizumab (Avastin). Ophthalmology 114, 855–859 (2007).
- R. K. Ucgul, S. Celebi, N. S. Yilmaz, N. Bukan, A. Y. Ucgul, Intrastromal versus subconjunctival anti-VEGF agents for treatment of corneal neovascularization: A rabbit study. Eve 35, 3123–3130 (2021).
- 42. V. Hampshire, S. Robertson, Using the facial grimace scale to evaluate rabbit wellness in post-procedural monitoring. *Lab Anim.* **44**, 259–260 (2015).
- Y. Jiang, B. Tian, Inorganic semiconductor biointerfaces. Nat. Rev. Mater. 3, 473–490 (2018).

Acknowledgments: C.H.L. acknowledges the Leslie A. Geddes Endowment at Purdue University, Y.M.P. acknowledges unrestricted departmental support from Research to Prevent Blindness. This work used the Vision Research Core Center funded by P30EY007003 from the National Eve Institute, W.P. acknowledges the Leslie Bottorff Fellowship Program at Purdue University. We acknowledge the donation of New Zealand White rabbits from the Center for Advanced Models and Translational Sciences and Therapeutics (CAMTraST) at the University of Michigan. We would like to thank K. Ejendal for sharing her expertise with in vitro experiments and antibody analysis and T. Qian for actively participating in the rabbit experiments. Funding: C.H.L. and Y.M.P. acknowledge funding support from the NIH National Eve Institute (NEI) (award number R01EY033000). C.H.L. also acknowledges the National Science Foundation (NSF) Chemical, Bioengineering, Environment, and Transport Systems (CBET) (award number 2032529). Y.M.P. also acknowledges the funding support from the NIH NEI (award numbers 1K08EY027458 and 1R41EY031219) along with the unrestricted departmental support from Research to Prevent Blindness. This work used the Vision Research Core Center funded by P30EY007003 from the NEI. D.R.K. acknowledges the funding support from the International Research and Development Program (NRF-2018K1A3A1A32055469) through the National Research Foundation of Korea (NRF) funded by the Ministry of Science and ICT of Korea, Y.J. acknowledges the funding support from the MOTIE (Ministry of Trade, Industry, and Energy) in Korea, under the Fostering Global Talents for Innovative Growth Program (P0008748, Global Human Resource Development for Innovative Design in Robot and Engineering) supervised by the Korea Institute for Advancement of Technology (KIAT). Author contributions: Y.M.P., D.R.K., and C.H.L. conceived the concept, planned the project, and supervised the research, W.P., Y.J., B.K., J.Y., H.K., D.R.K., and C.H.L. conducted experiments and data analysis on the ocular drug delivery platform. V.P.N. Y.L., and Y.M.P. designed, fabricated, and characterized animal studies, J.W.L. and Y.L.K. conducted experiments and data analysis on the optical haze of lenses. W.P., V.P.N., Y.J., D.R.K., Y.M.P., and C.H.L. wrote the manuscript. All authors commented on the paper. Competing interests: Y.M.P., D.R.K., and C.H.L. are inventors on a U.S. provisional patent related to this work filed by Purdue University Office of Technology Commercialization (no. 63/253,686) entitled "Ocular drug delivery devices and methods of fabrication and use therefore." The authors declare no other competing interests. Data and materials availability: All data needed to evaluate the conclusions in the paper are present in the paper and/or the Supplementary Materials.

Submitted 8 November 2021 Accepted 8 February 2022 Published 30 March 2022 10.1126/sciady.abn1772

# **Science** Advances

# Biodegradable silicon nanoneedles for ocular drug delivery

Woohyun Park, Van Phuc Nguyen, Yale Jeon, Bongjoong Kim, Yanxiu Li, Jonghun Yi, Hyungjun Kim, Jung Woo Leem, Young L. Kim, Dong Rip Kim, Yannis M. Paulus, and Chi Hwan Lee

Sci. Adv., **8** (13), eabn1772. DOI: 10.1126/sciadv.abn1772

View the article online

https://www.science.org/doi/10.1126/sciadv.abn1772

**Permissions** 

https://www.science.org/help/reprints-and-permissions

Use of this article is subject to the Terms of service

to original U.S. Government Works. Distributed under a Creative Commons Attribution NonCommercial License 4.0 (CC BY-NC).